arXiv:2404.11378v1 [cond-mat.other] 17 Apr 2024

Hexagonal quasiperiodic tilings as decorations of periodic lattices

Sam Coates[1]

[1]*Surface Science Research Centre and Department of Physics, University of Liverpool, Liverpool L69 3BX, UK*[*]

(Dated: April 18, 2024)

Symmetry sharing facilitates coherent interfaces which can transition from periodic to quasiperiodic structures. Motivated by the design and construction of such systems, we present hexagonal quasiperiodic tilings with a single edge-length which can be considered as decorations of a periodic lattice. We introduce these tilings by modifying an existing family of golden-mean trigonal and hexagonal tilings, and discuss their properties in terms of this wider family. Then, we show how the vertices of these new systems can be considered as decorations or sublattice sets of a periodic triangular lattice. We conclude by simulating a simple Ising model on one of these decorations, and compare this system to a triangular lattice with random defects.

I. INTRODUCTION

Quasiperiodic tilings have been well-studied across the range of the physical sciences. They can be used as simple tools to better understand or generate quasicrystalline phases of matter, studied as intrinsic mathematical objects, or utilised in applied research as the basis for fabricated/manipulated structures. Historically, focus has been applied to such tilings which exhibit rotational symmetries which are incommensurate with periodicity or translational symmetry: 5-, or greater than 6-fold. However, this is not a required condition – quasiperiodic tilings can, of course, be 2-, 3-, 4-, or 6-fold [1–9].

The sharing of symmetries opens the door to coherent periodic-to-quasiperiodic interfaces, as it is the gateway to reducing or minimizing structural frustration. For example: decorating a 3-fold symmetric lattice with a 5-fold symmetric pattern, or sandwiching together 3-fold and 5-fold structures results in heterogeneous or incommensurate interactions between the two systems. On the other hand, periodic and quasiperiodic structures could mix in a more systematic manner if their local environments are cohesive. The motivation for this work stems from this idea, in which we focus on 6-fold quasiperiodic tilings. We choose this symmetry as hexagonal (and trigonal) structures have the highest coordination number for a 2D periodic lattice (6), and therefore offer a more 'flexible' local neighbourhood for manipulation.

Previously, we have introduced a family of hexagonal and trigonal tilings using a generalised version of de Bruijn's dual grid method [10–17]. The structure of the tilings could be controlled by two parameters, α_s and α_l, such that we labelled our tilings as $H_{\alpha_s\alpha_l}$. Each tiling consisted of hexagonal and/or rhombic tiles with edge lengths built by the linear combination of two length-scales: 1 and $\tau = \frac{1+\sqrt{5}}{2}$. In this work we paid particular attention to two 'special' cases in this family, which we referred to as H_{00} and $H_{\frac{1}{2}\frac{1}{2}}$.

[*] Corresponding author: samuel.coates@liverpool.ac.uk

Here, we modify the construction of the H_{00} and $H_{\frac{1}{2}\frac{1}{2}}$ systems with a view to generate single edge-length hexagonal (SEH) quasiperiodic tilings. The single edge-length parameter more readily leads to periodic-to-quasiperiodic interfaces with relatively simple local environments – and is an advantage for both physical and theoretical realisations. First, we show the basic method used to construct the SEH tilings and compare them to their H_{00} and $H_{\frac{1}{2}\frac{1}{2}}$ counterparts. Then, we present the structural properties of the SEH_{00} and $SEH_{\frac{1}{2}\frac{1}{2}}$ tilings in their own right in terms of their vertices, discuss their relationship to periodic lattices, and illustrate the many variations that can be constructed by deliberate and/or creative choices. Next, to demonstrate some physical properties of these systems, we present the results of a simple Ising spin system simulated on the SEH_{00} tiling. We conclude by briefly discussing potential applications across multiple length-scales.

II. CONSTRUCTION OF THE *SEH* TILINGS

Here, we briefly discuss de Bruijn's dual grid method in accessible terms, with the aim of introducing the relevant parameters for the formation of the H and SEH tilings. Then, we move on to presenting the SEH tilings, compare them to the H tilings, and highlight the creative possibilities afforded by changing scaling parameters.

de Bruijn's method and the H tilings

An infinite set of regularly-spaced parallel lines defines a grid, where the spacing and orientation of the grid lines is determined by a perpendicular grid vector $\mathbf{k}^{(j)}$. A multigrid is then composed of a set of grids, with grid vectors $\mathbf{k}$. A particular tiling is dual to this multigrid in the sense that the intersection points of grids directly correspond to tiles in a tiling space. These tiles are formed by the tiling vectors $\mathbf{a}$, which belong to the same family of the grids involved in the intersection. In other words, if grids j and $j+1$ intersect, the corresponding tile is

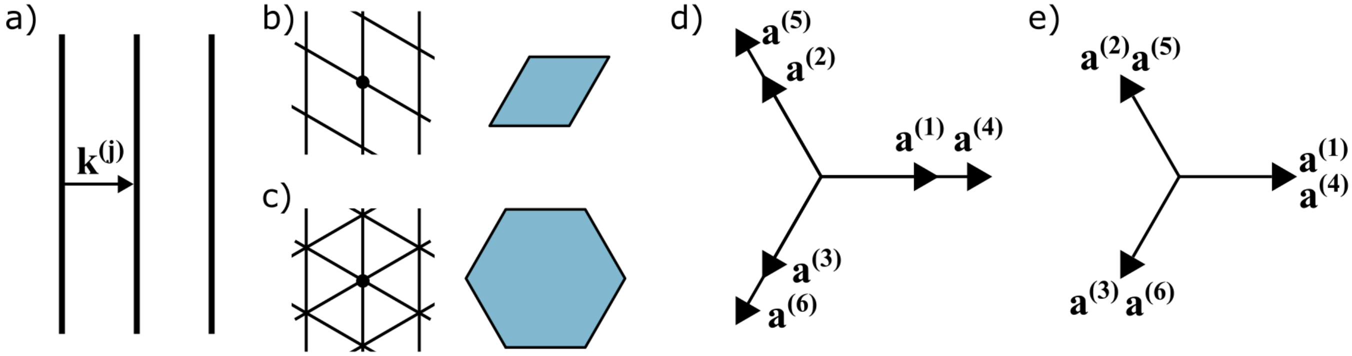

FIG. 1: **(a)** Three parallel lines indicate a section of an infinite grid. The spacing and orientation of the grid lines is defined by the perpendicular grid vector $\mathbf{k}^{(j)}$. **(b)** A singular intersection point between two sets of grids defined by $\mathbf{k}^{(1)}$ and $\mathbf{k}^{(2)}$ corresponds to a rhombic tile created by the associated tiling vectors $\mathbf{a}^{(0)}$ and $\mathbf{a}^{(1)}$. **(c)** A regular intersection point results in a polygon with the number of edges (6) equal to twice the number of grids involved in the intersection (3). **(d)** The $\mathbf{a}$ vectors associated with the H tilings. $\mathbf{a}^{(1-3)}$ are a factor of τ shorter than $\mathbf{a}^{(4-6)}$. **(e)** The $\mathbf{a}$ vectors associated with the SEH tilings. The lengths of all $\mathbf{a}$ are set to 1.

formed of vectors $\mathbf{a}^{(j)}$ and $\mathbf{a}^{(j+1)}$. When two grids intersect at a point (*regular*), the resultant tile is rhombic. When more than two intersect (*singular*), a polygonal tile is formed, with the number of edges equal to twice the number of grids involved in the intersection. Figures 1(a − c) demonstrate the relationship between $\mathbf{k}$ and its grid, examples of regular and singular multigrids, and the resultant tiles formed by their intersection points.

Rather than reiterating the comprehensive approach we took to defining our previous family of tilings [8], we simply state their vector families and associated parameters. Gähler and Rhyner showed under the generalised dual grid method that the choice of tiling and grid vectors need not be identical – the only restriction being that both families of vectors span a volume of the same orientation [13]. So, following the notation of Rabson [15, 16], our grid and tiling vectors were defined using unit vectors:

$$\mathbf{n}^{(j)} = \left(\cos\frac{2\pi(j-1)}{3}, \sin\frac{2\pi(j-1)}{3}\right), \quad j = 1, \dots 6, \tag{1}$$

such that our grid vectors were:

$$\mathbf{k}^{(j)} = \frac{2\pi}{L_j}\mathbf{n}^{(j)}, \quad j = 1, \dots 6, \tag{2}$$

and our tiling vectors were:

$$\mathbf{a}j = \frac{2\tau}{3\sqrt{5}}\frac{1}{L_j}\mathbf{n}^{(j)}, \quad j = 1, \dots 6, \tag{3}$$

where L_j defines the scaling of our vectors:

$$L_j = \begin{cases} \tau, & j = 1, 2, 3, \\ 1, & j = 4, 5, 6. \end{cases} \tag{4}$$

Essentially, as one can choose the scale of the vectors freely [13], we separated our grid and tiling vectors into two groups. We chose $\mathbf{a}^{(1-3)}$ to be a factor of τ shorter than $\mathbf{a}^{(4-6)}$, as shown in Figure 1(d), and the spacing between grids $\mathbf{k}^{(1-3)}$ to be a factor of τ longer than $\mathbf{k}^{(4-6)}$. This meant that the grids associated with the longer tiling vectors $\mathbf{a}^{(4-6)}$ were crossed more often, and, as a consequence, 'large' tiles appear more frequently – as expected in Fibonacci or golden-mean tilings [18]. Although our work focussed on τ-scaled tilings, we also demonstrated that any irrational constant could be used (as expected from [13]).

Finally, the two parameters mentioned earlier, α_s and α_l, correspond to the sum of translational shifts applied to the grids f_j along the direction of the grid vectors $\mathbf{k}^{(j)}$, such that:

$$\alpha_s = f_1 + f_2 + f_3 \quad \text{and} \quad \alpha_l = f_4 + f_5 + f_6, \tag{5}$$

where -1 $\leq f_j \leq$ 1. Figures 2(a) and (b) show examples of tilings where $\alpha_s \equiv \alpha_l \equiv 0$, and $\alpha_s \equiv \alpha_l \equiv 0.5$, or, the H_{00} and $H_{\frac{1}{2}\frac{1}{2}}$ tilings, respectively. The H_{00} tiling is comprised of 3 tiles: a small hexagon (edge length = 1), a parallelogram (edge lengths = 1, τ), and a large hexagon (edge length = τ). The $H_{\frac{1}{2}\frac{1}{2}}$ tiling is technically built using two mirror-symmetric parallelogram tiles, three small, and three large rhombuses. However, the colour scheme of Figure 2(b) is simplified as the specific properties of these tiles are not discussed here.

The *SEH* tilings

In the simplest terms, under the dual grid method, the placement or arrangement of tiles is determined by the multigrid intersection points. So, the arrangement of tiles in the H_{00} and $H_{\frac{1}{2}\frac{1}{2}}$ tilings is quasiperiodic due

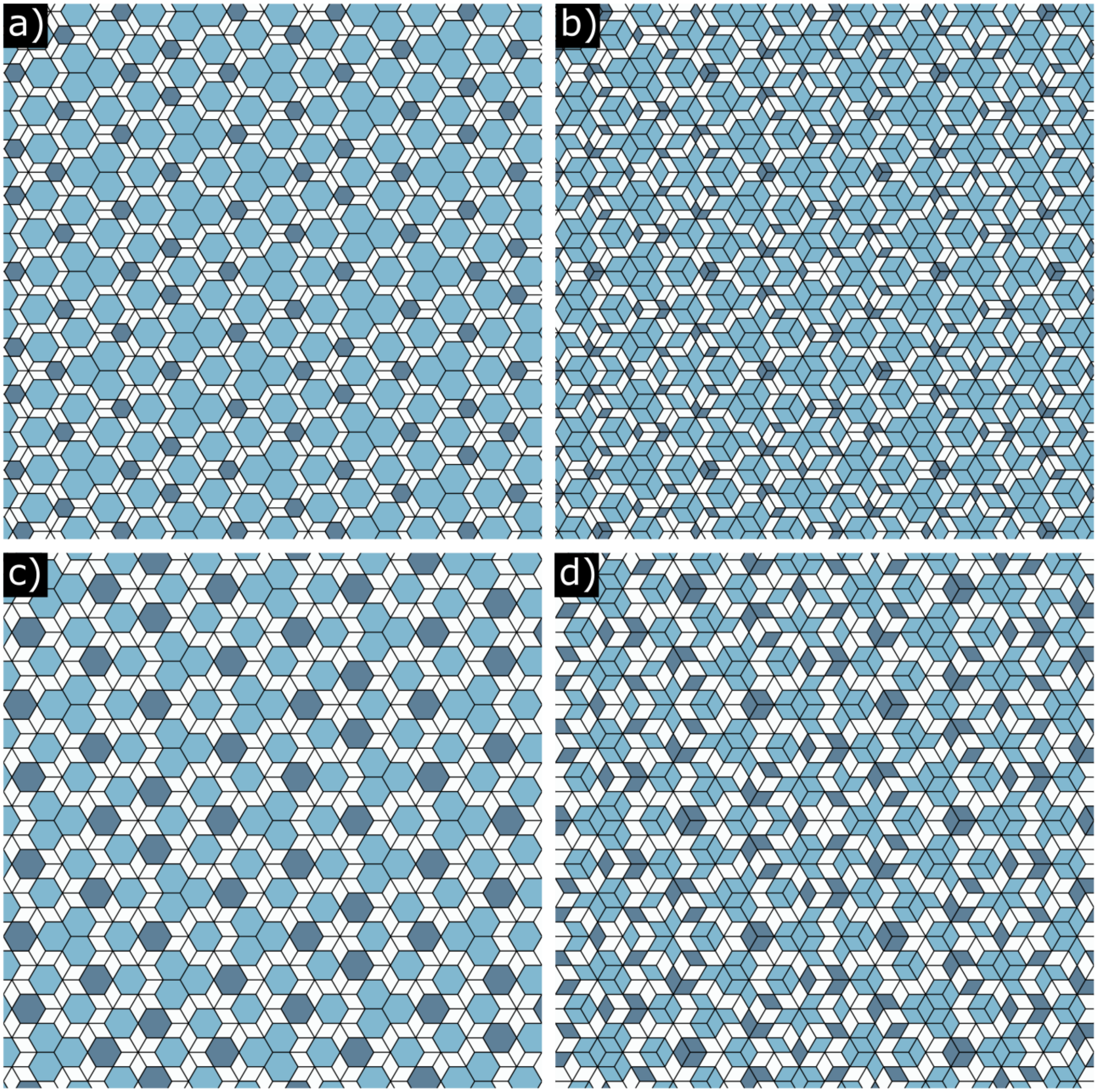

FIG. 2: **(a)** The H_{00} tiling, where $\mathbf{a}^{(1-3)}$ are a factor of τ shorter than $\mathbf{a}^{(4-6)}$, and the shifts applied to the grids sum to 0. **(b)** The $H_{\frac{1}{2}\frac{1}{2}}$ tiling, where the shifts applied to the grids sum to 0.5. **(c)** The SEH_{00} tiling, where the length of all $\mathbf{a} = 1$, and the shifts applied to the grids sum to 0. **(d)** The $SEH_{\frac{1}{2}\frac{1}{2}}$ tiling, where the shifts applied to the grids sum to 0.5.

to the irrational scaling factor between the two sets of grid vectors $\mathbf{k}^{(1-3)}$ and $\mathbf{k}^{(4-6)}$. The tiling vectors, however, only affect the geometry of the tiles. Therefore, as long as the scaling factor between the two groups of grid vectors is irrational, we can simply set the scaling factor of the tiling vectors to be 1 and produce a hexagonal quasiperiodic arrangement of single edge-length tiles.

Keeping our focus on systems where $\alpha_s \equiv \alpha_l \equiv 0$, and $\alpha_s \equiv \alpha_l \equiv 0.5$, Figures 2(c, d) show the SEH_{00} and $SEH_{\frac{1}{2}\frac{1}{2}}$ tilings, which are generated by keeping the scaling factor between $\mathbf{k}^{(1-3)}$ and $\mathbf{k}^{(4-6)}$ as τ, and setting the lengths of $\mathbf{a} = 1$, as in Figure 1(e). The colour scheme of individual tiles is kept constant under this change, for clarity. Decreasing the scale of tiling vectors $\mathbf{a}^{(4-6)}$ de-

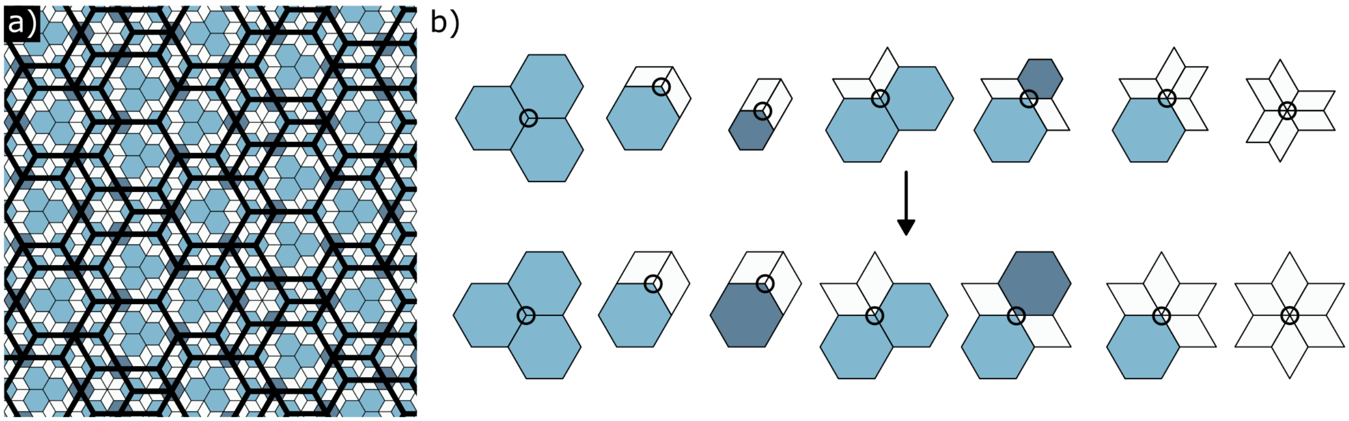

FIG. 3: **(a)** A H_{00} tiling (thick black lines) with short and long tile edge lengths of 2 and 3 can be overlaid on isolated hexagonal tiles of the SEH_{00} tiling. **(b)** Top: the seven vertex configurations of the H_{00} tiling. Bottom: the corresponding vertices in the SEH_{00} tiling.

creases the longer parallelogram edges of H_{00} and $H_{\frac{1}{2}\frac{1}{2}}$ to form rhombuses, while the larger hexagons in H_{00} and rhombuses in $H_{\frac{1}{2}\frac{1}{2}}$ shrink to match the size of their smaller counterparts.

Comparing the H and SEH tilings, it is trivial that scale independent properties such as tile frequency and edge-matching rules still hold. This is also true for the vertex frequencies, however, we will discuss the vertices and their properties separately in the next section. The substitution rules we have previously discussed for the H tilings are no longer valid [8], as we have lost the self-similar scaling factor of τ; whether the SEH tilings have discrete substitution rules is an open topic. Out of interest, we note a perhaps obvious mapping or decoration property of the SEH_{00} tiling. Figure 3(a) shows that isolated hexagonal tiles i.e., those not connected to other hexagons by an edge, can be decorated with a H_{00} tiling where the ratio of the long to short edge lengths of tiles is 3/2, an approximation of τ. When we decorate the same 'parental' tiles in the τ-scale H_{00} tiling, we find it forms a τ^2 inflated version of the original, where the tiles have edge lengths $2+\tau$ and $1+\tau$. Therefore, as we shrink $\tau \to 1$ to create the SEH_{00} tiling, we create a 3:2 ratio. A similar mapping likely holds for the $SEH_{\frac{1}{2}\frac{1}{2}}$ tiling.

III. *SEH* TILING VERTICES AND PERIODIC LATTICE DECORATIONS

In this section, we will briefly present observations on the properties of the vertex configurations of the hexagonal tilings under the shrinking of $\mathbf{a}^{(4-6)}$, before moving on to discuss the considering the SEH tilings as decorations of periodic triangular lattices.

Vertex configurations

The top of Figure 3(b) shows the seven vertex configurations of the H_{00} tiling [8], and the bottom shows the corresponding vertices in the SEH_{00} tiling. The properties of these vertices are scale independent – changing the tile edge lengths does not affect the number of vertex types, nor their frequency across the tiling, as these are determined in grid-space. The same is true for the $H_{\frac{1}{2}\frac{1}{2}}$ tiling – for conciseness however we do not show these; the $H_{\frac{1}{2}\frac{1}{2}}$ tiling has 32 vertex types. This leads us to the observation that we should expect identical magnetic behaviour to previous work on the magnetic states of the H_{00} and $H_{\frac{1}{2}\frac{1}{2}}$ tilings under the Hubbard model [19, 20] – as in these cases we considered equal hopping interactions between vertices separated by non-equal edge lengths.

Analysis of vertices in a quasiperiodic tiling is commonly done by considering the points as projections from a higher-dimensional superspace. Indeed, we previously showed how both the H_{00} and $H_{\frac{1}{2}\frac{1}{2}}$ tilings can be constructed via the projection of a hypercubic lattice. The basis of this lattice was defined by a matrix of six orthogonal 6-dimensional vectors, whose first two rows contain the tiling vectors $\mathbf{a}$ [[8], section IV]. For the SEH tilings, we can still view the vertices as projections onto an internal subspace using the same matrix, such that the internal subspace windows and their subdivisions are identical to the H tilings. In this case, we do not obtain any new information by considering the SEH tilings in hyperspace. However, as we have altered $\mathbf{a}$, the original matrix no longer describes an orthogonal hypercubic lattice.

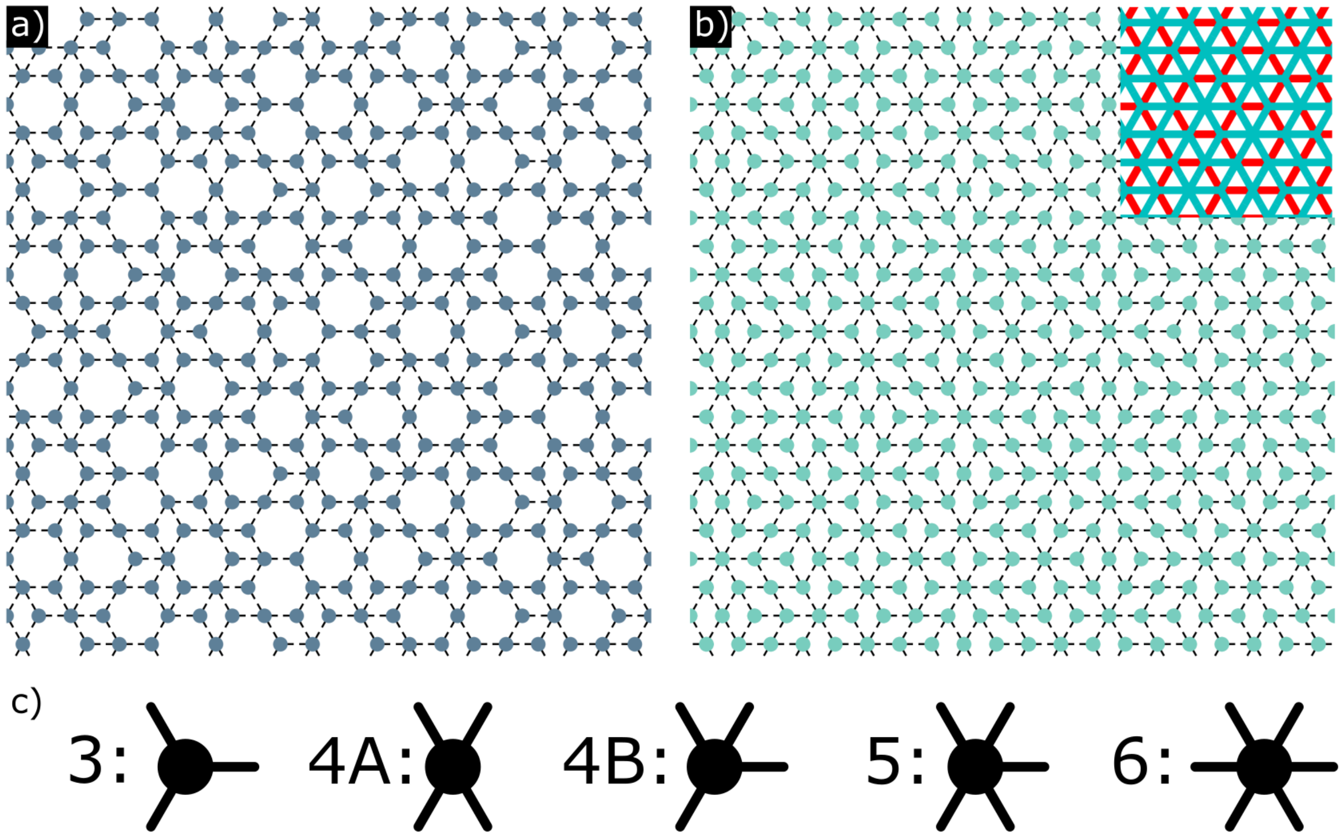

FIG. 4: **(a, b)** The vertex schematics of the SEH_{00} and $SEH_{\frac{1}{2}\frac{1}{2}}$ tilings, where the edges of tiles have been bisected. Under this scheme, the tilings can be considered as positions by 'bonds'. Inset in **(b)** is an overlay of a periodic triangular tiling (cyan), where certain edges are coloured red. These edges, when removed, form the $SEH_{\frac{1}{2}\frac{1}{2}}$ tiling. **(c)** The five n-vertex types associated with the tilings under the bond picture. Each type is labelled according to their coordination number.

SEH **vertices as periodic lattice decorations**

The vertices of the SEH tilings can be directly related to periodic triangular lattices. Figures 4(a, b) show the vertices of the SEH_{00} and $SEH_{\frac{1}{2}\frac{1}{2}}$ tilings respectively, where the edges of the tiles have been bisected to illustrate the relationship to periodic lattices and the connectivity between adjacent vertices.

This relationship is clearest for the $SEH_{\frac{1}{2}\frac{1}{2}}$ tiling, where each vertex perfectly decorates a periodic triangular lattice with a lattice constant of 1. Under this scheme, it becomes clear that the tile edges or bonds between vertices are quasiperiodic, while the vertex or point distribution is not. Therefore, an alternative way to produce the $SEH_{\frac{1}{2}\frac{1}{2}}$ tiling would be to remove a subset of edges from a perfect triangular lattice tiling. An example is overlaid and inset in Figure 4(b), where the cyan lines indicate the triangular lattice, and the red lines are edges which are removed. The centre point of these removed edges sit at the centre of the $SEH_{\frac{1}{2}\frac{1}{2}}$ tiles, such that if we produce the dual tiling of the $SEH_{\frac{1}{2}\frac{1}{2}}$ tiling, its vertices consist of 'removal' points. Overlaying this dual on top of a periodic triangular tiling then provides a guide for which edges to remove in order to produce the $SEH_{\frac{1}{2}\frac{1}{2}}$ tiling. We show the dual in appendix A 1, which contains triangular, rectangular, pentagonal, and hexagonal tiles with edge lengths $\frac{\sqrt{3}}{2}$ and 1. The SEH_{00} vertices also decorate a triangular lattice, albeit with additional quasiperiodically spaced 'vacancies' which arise from the centre of the hexagonal tiles[1]. These vacancies can be considered as perfectly ordered defects in a triangular lattice – a property we explore in the following section. Similar to the $SEH_{\frac{1}{2}\frac{1}{2}}$ tiling, we can produce a dual using the centres of the removed edges, which is also shown in appendix A 1.

The relationship of the SEH tilings to periodic lattices represents a potential route into exploring bespoke quasiperiodic arrangements whose local environments are commensurate with periodic structures. Similarly,

[1] These vacancies can also form a decorated 3:2 ratio H_{00} tiling.

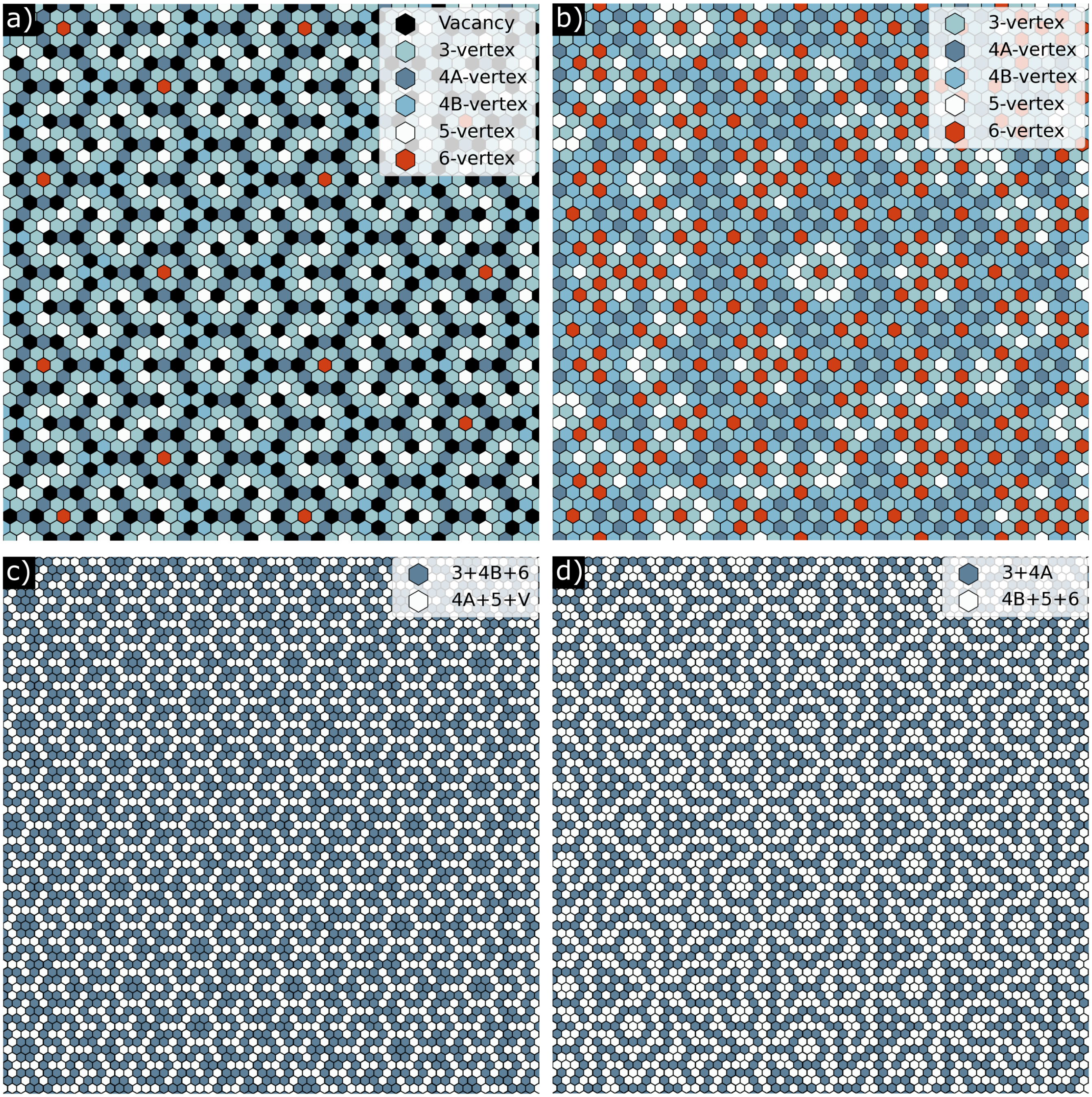

FIG. 5: **(a, b)** n-vertex models of the SEH_{00} and $SEH_{\frac{1}{2}\frac{1}{2}}$ tilings, respectively. Here, each vertex has been colour-coded depending on their coordination number, with an additional vacancy position added at the centre of the hexagonal tiles in the SEH_{00} tiling. The points occupy separate sublattices of a periodic triangular lattice. **(c, d)** Bipartite systems formed by the combination of specific vertex types on the SEH_{00} and $SEH_{\frac{1}{2}\frac{1}{2}}$ tilings, respectively. The vertex types used are indicated in the legends.

one can imagine designing interfaces which more readily broach the gap between periodic/quasiperiodic systems, which we will discuss in further work. To demonstrate the many structures which can be obtained for such work, we characterize the SEH tiling vertices as quasiperiodic decorations of a periodic lattice. To do so, we classify each tiling vertex with respect to their coordination number, and then consider these as separate quasiperiodic sublattices which occupy a periodic lattice.

The five resultant vertex types which comprise the two tilings in this form are shown in Figure 4(c); we refer to them as n-vertices, where n is their coordination number. It is worth noting that we have collated all vertices that are comprised of 3 vectors; technically, according to Figure 3(b) there are three distinct 3-vertex types in the SEH_{00} tiling (and many more in the $SEH_{\frac{1}{2}\frac{1}{2}}$). However, in this section we are more focussed on characterising and discussing the connectivity between geometrically unique sites (in terms of 'bonds'), so, for simplicity's sake, we group these together. For the two 4-vertices, we label them 4A and 4B, as they are geometrically unique. Out of interest, we note that the vertices in Figure 4(c) look similar to the schematic representations of patchy particles studied in self-assembly systems [21]. Whether the vertices we present here could theoretically or experimentally self-assemble – similar to other patchy particle/tiling work [22–26] – is an intriguing question for future work.

Figures 5(a, b) show the SEH_{00} and $SEH_{\frac{1}{2}\frac{1}{2}}$ distributions of the n-vertices respectively, colour-coded with respect to their n-vertex type, and plotted as hexagons for clarity. For the SEH_{00} tiling, we plot the centre of the hexagonal tiles as 'vacancies'. These figures serve to illustrate the wide range of decorations or designs available for investigation; for reference, we plot the radial distribution functions for each vertex type in appendix A 2. In the simplest sense, we can construct bipartite systems using distinct sublattices by combining certain n-vertex types. For the SEH_{00} tiling, we have 6 types of vertices that can be combined to give 31 unique two-part structures – calculated by summing the binomial coefficients and removing the combination where all vertices are selected. Correspondingly, the SEH_{00} tiling has 15 unique types. We note that if we were to consider all instances of the 3-vertices as occupying separate sublattices, the number of available combinations increases dramatically.

Figures 5(c, d) show selected examples of such combinations for the SEH_{00} and $SEH_{\frac{1}{2}\frac{1}{2}}$ tilings respectively, chosen only for their aesthetic quality; for reference, the remaining combinations for both tilings are shown in appendix A 3. Similarly, and importantly, both the ratio and arrangement of these n-vertices can be altered by changing the irrational scaling constant between $\mathbf{k}^{(1-3)}$ and $\mathbf{k}^{(4-6)}$. We show a few additional examples with different constants in appendix A 4. Of course, creative choices can be made using any irrational constant and/or selection of n-vertices as ingredients to design quasiperiodic structures either spontaneously, or, with desired structural environments/properties in mind. We note that the combinatorial sub-lattice selection method we have used here could also be applied to the Fibonacci square tiling, or to the marked supertiles of the 'Spectre' monotile, for instance [3, 27].

IV. ISING MODEL ON THE SEH_{00} TILING

As previously mentioned, the SEH_{00} vertices can be considered as a triangular lattice with a quasiperiodically ordered set of vacancy defects. Now, the effect of topological defects on magnetic properties is a highly active field – particularly with regards to hexagonal structures [28–33]. As such, this system presents a potentially important stepping stone on the structural order spectrum between a perfectly crystalline triangular lattice and one with randomly ordered defects. Here, we choose to briefly explore the magnetic states of structures across this spectrum under a simple Ising model[2].

Simulation method

We study the J_1-J_2 Ising model on our systems using the Monte Carlo method, such that our Hamiltonian is:

$$H = J_1 \sum_{\langle ij \rangle} \vec{S}_i \cdot \vec{S}_j + J_2 \sum_{\langle\langle ij \rangle\rangle} \vec{S}_i \cdot \vec{S}_j \tag{6}$$

where J_1 and J_2 are the nearest- and next-nearest neighbour interactions, NN and NNN respectively, for sites i and j with spins S_i and S_j. Spins can either be up $\binom{0}{1}$ or down $\binom{0}{-1}$. We investigate the system in two states: considering $J_1 = -1$, and $J_2 = 1, -1$. In other words, NN is set to be antiferromagnetic, and we modify NNN to either be ferromagnetic or antiferromagnetic.

For each structure type, we use a square patch containing approximately 1500 spins, without periodic boundary conditions. We run the Monte Carlo simulation over 45 descending temperatures, normalised by the lowest energy for a single site (T/J) on the triangular lattice. For each temperature, we attempt 10^6 spin flips. Each structure is simultaneously simulated 10 times, and we average the results over the ensemble. To ensure 'sensible' results for the SEH_{00} and defect structures, we compare the final spin states of the triangular lattice under each J_1-J_2 to those well known in the literature [34, 35].

Finally, the random defect models are constructed by inspecting the properties of vacancies in Figure 5(a); no two vacancies touch, and they constitute around 19% of all vertices. We iteratively and randomly removed points from a triangular lattice until these conditions are met. An example of the vertex distribution and 'random tiling' model of one of these defect lattices is shown in appendix B.

Results and analysis

Figure 6 shows a summary of our results: Figures 6(a-c) are where $J_1 \equiv J_2 \equiv -1$, and Figures 6(d-f) where

[2] The $SEH_{\frac{1}{2}\frac{1}{2}}$ vertices form a perfect triangular lattice, as discussed, which is an Ising system that has widely been studied. However, it should be mentioned that the properties of the $SEH_{\frac{1}{2}\frac{1}{2}}$ tiling can still be explored (for any Hamiltonian) if we consider interactions allowed only along tile edges (as with the Hubbard model [19, 20])

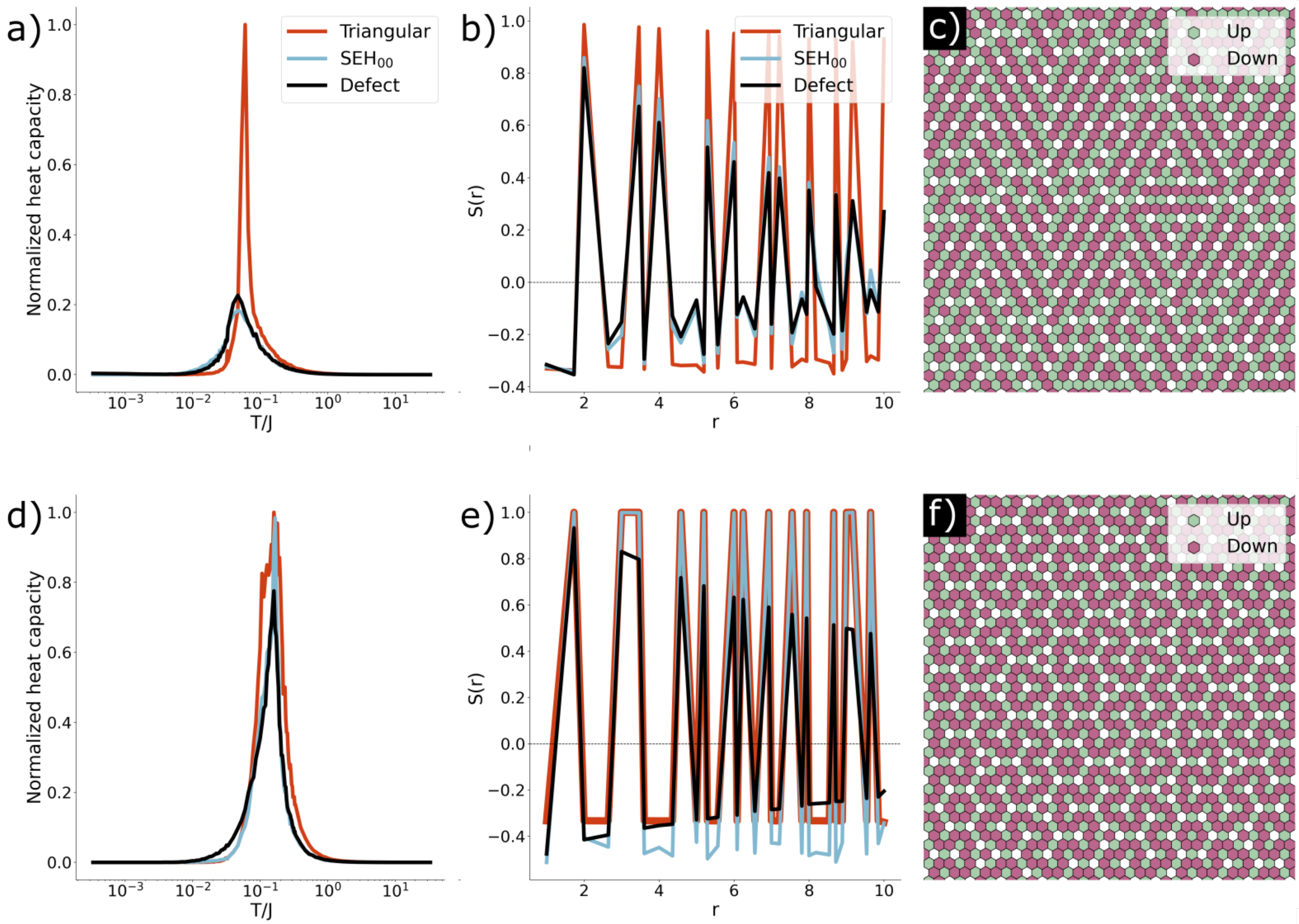

FIG. 6: **(a-c)**: results where $J_1 = J_2 = -1$. **(d-f)**: where $J_1 = -1$, $J_2 = 1$. **(a, d)** Heat capacity of the spin systems, which have been averaged over the ensemble and normalized by the maximum value across the three structures. **(b, e)** Spin correlation functions according to Eq. 8 for the final spin states across the ensemble. **(c, f)** Randomly chosen spin textures of final spin states on the SEH_{00} tiling vertices, which are colour-coded by spin and plotted as hexagons.

$J_1 = -1, J_2 = 1$, which we discuss separately below. Figures 6(a, d) show the temperature dependent heat capacity, C, which is calculated by:

$$C(T) = \frac{(\langle E^2 \rangle - \langle E \rangle^2)}{T} \tag{7}$$

where the energy of each system is sampled at regular intervals per T, and C has been normalized by the maximum value across the three systems.

Figures 6(b, e) show a spin-spin correlation function:

$$S(r) = \langle \vec{S}_i \cdot \vec{S}_r \rangle \tag{8}$$

where r is the distance between two spins, which we calculate for up to 10 distance units. For instance, if all spins for a certain r are aligned parallel, $S(r) = 1$, while if they are anti-parallel $S(r) =$ -1. Finally, Figures 6(c, f) show randomly selected final spin-states. We have plotted the spins on the SEH_{00} vertices as hexagons, which are colour-coded to represent their spin direction.

$$J_1 \equiv J_2 \equiv -1$$

Figure 6(a) shows that the triangular lattice has a clear sharp peak according to the phase transition from a disordered to an ordered stripe-phase spin system. For the SEH_{00} and defect systems this transition occurs at a lower T, and the peaks are smaller and broader. As the relatively small peak height means these systems require less heat to undergo a phase transition, it may suggest that they are also less stable than the triangular phase. The broadness of the peaks indicates a comparatively frustrated system to the triangular lattice: frustration impedes long-range ordering, which causes the system to

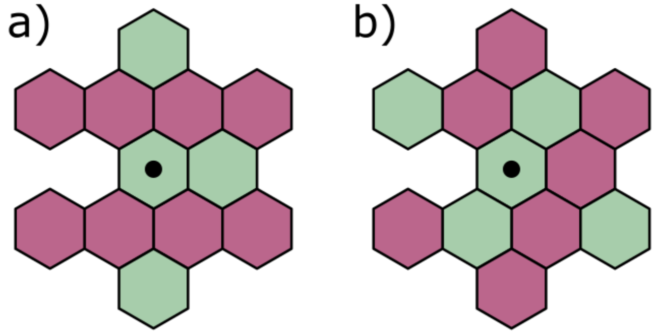

FIG. 7: Lowest energy states when $J_1 \equiv J_2 \equiv -1$ for the 5-vertex considering Eq. 6 on the vertex only **(a)**, and across the whole vertex neighbourhood **(b)**.

explore a wider range of spin configurations.

Figure 6(b) shows clear long-range order on the triangular lattice: $S(r)$ oscillates between 1 and -$\frac{1}{3}$ as expected for the stripe phase – with some variance which is caused by small coexisting stripe phases with different orientations. For the SEH_{00} and defect spins, however, $S(r)$ decreases with increasing r, indicating systems with less long-range order. This can be seen in Figure 6(c): while the spin structure consists of the striped-phase of the triangular lattice, the orientation of the stripes is not continuous across the system (the same occurs for the defect system). This can be explained by considering the 5-vertex spin neighbourhoods which occur in both the SEH_{00} and defect structures, and appear to influence the orientation of the stripes. The 5-vertex positions have six NNN, meaning that they feel the largest spin pressure compared to the other vertices (in other words, they are surrounded by 11 interacting spins), and are therefore perhaps the most important positions to satisfy energetically.

Figure 7 shows the two lowest-energy states on the 5-vertex: Figure 7(a) considers Eq. 6 on the vertex *only*, while Figure 7(b) considers it across the whole neighbourhood. The striped phase on these vertices is clear to see, however, the direction is rotated by 120° between the two. Similarly, the orientation of the 5-vertex is 6-fold across the system, determined by the position of the vacant spin. The multiple orientations of striped phases seen in Figure 6(c) are therefore likely caused by a mixture of the competition between the two low-energy states and the many 5-vertex orientations across the system. Whether the stripe phase domain sizes or orientations can be tuned by changing the arrangement of the 5-vertices is an open question.

$$J_1 = -1, J_2 = 1$$

Figure 6(d) shows that the phase transition for all three systems occurs at the same T, and that the heat capacity of the triangular and SEH_{00} structures have nearly the same peak height. In fact, the sharp shape and smaller full-width half-maximum of the SEH_{00} peak indicates a system which potentially holds less frustration than the other spin-structures. Similarly, Figure 6(e) shows that the SEH_{00} spins have perfect long-range order in contrast to the defect system; the larger magnitude $S(r)$ value for anti-parallel spins (~ -0.45) compared to the triangular lattice ($-\frac{1}{3}$) arises simply from the reduction in the average number of NN and NNN spins.

The long-range structure of the system is driven by the fact that there are positions in the SEH_{00} tiling which can perfectly decorate the points of a periodic triangular lattice with a lattice constant of 2. These sites are occupied by up spins in Figure 6(f), and are fully satisfied energetically: their NN are anti-parallel, and their NNN are parallel. As for frustration, the vacant positions in Figure 6(f) would be down spins on the triangular lattice – as such they would have three unfavourable parallel and three favourable anti-parallel NN spins. Likewise, they would represent an unfavourable parallel spin in a neighbouring down spin site. The 'removal' of these sites therefore reduces the overall frustration of the system.

V. CONCLUSIONS AND OUTLOOK

We have introduced two single edge-length quasiperiodic tilings, produced by the dual-grid method. As a consequence we have presented a quasiperiodic system of vertices or sublattices which can be considered as decorations on a periodic lattice. Lastly, we have shown some rudimentary magnetic properties of these systems.

As a general comment on our theoretical magnetic investigation with a view to future work, we note we have only explored two extremes of a simple toy system. However, the behaviour of the SEH_{00} tiling at these two extremes (similar to a random defect model at $J_2 = -1$, less frustrated than a triangular lattice at $J_2 = 1$) indicates a potentially rich magnetic phase diagram to explore, particularly with ordered/disordered vacancy defects in mind. Likewise, investigating xy- or xyz-spins, considering our system as a dimer model [36–39] , or physical manifestations [29, 40] suggests a range of possible further work.

The quasiperiodic decorations we have presented suggest wide and flexible experimental opportunities, and allows for the investigation of interfacial quasiperiodic/periodic arrangements which have minimized spatial frustration. The decorations we have shown could be realised and explored at multiple length scales, with examples not limited to: manipulated adsorbate/defect systems on a hexagonal close packed surface [41–44], photonic materials with different dielectric constants [45–48], scatters in waveguides [49–56], or as mechanical metamaterials [57–60].

VI. ACKNOWLEDGEMENTS

This work was supported by EPSRC grant EP/X011984/1. SC would like to thank J. A. Smerdon and P. Moriarty for useful discussions.

[1] V. Sasisekharan, S. Baranidharan, V. S. K. Balagurusamy, A. Srinivasan, and E. S. R. Gopal. Non-periodic tilings in 2-dimensions with 4, 6, 8, 10 and 12-fold symmetries. *Pramana*, 33(3):405–420, 1989.

[2] D. S. Clark and E. R. Suryanarayan. Quasiperiodic tilings with low-order rotational symmetry. *Acta Crystallogr. A*, 47(5):498–502, 1991.

[3] R. Lifshitz. The square Fibonacci tiling. *Journal of Alloys and Compounds*, 342(1):186–190, 2002.

[4] R. Lifshitz. Quasicrystals: A matter of definition. *Foundations of Physics*, 33:1703–1711, 2003.

[5] R. Lifshitz. What is a crystal? *Zeitschrift für Kristallographie*, 222(6):313–317, 2007.

[6] J. E. S. Socolar and J. M. Taylor. An aperiodic hexagonal tile. *J. Comb. Theory Ser. A*, 118(8):2207–2231, 2011.

[7] T. Dotera, S. Bekku, and P. Ziherl. Bronze-mean hexagonal quasicrystal. *Nature Mater.*, 16(10):987–992, 2017.

[8] S. Coates, A. Koga, T. Matsubara, R. Tamura, H. R. Sharma, R. McGrath, and R. Lifshitz. Hexagonal and trigonal quasiperiodic tilings, 2023.

[9] D. Smith, J. S. Myers, C. S. Kaplan, and C. Goodman-Strauss. An aperiodic monotile. *arXiv preprint arXiv:2303.10798*, 2023.

[10] N. G. de Bruijn. Algebraic theory of Penrose's non-periodic tilings of the plane (Parts I & II). *Proc. Kon. Ned. Akad. Wet. Ser. A*, 84:39–66, 1981. (Indag. Mathem., **43**).

[11] N. G. De Bruijn. Dualization of multigrids. *J. Phys. Colloques*, 47:C3–9, 1986.

[12] J. E. S. Socolar, P. J. Steinhardt, and D. Levine. Quasicrystals with arbitrary orientational symmetry. *Phys. Rev. B*, 32:5547–5550, 1985.

[13] F. Gahler and J. Rhyner. Equivalence of the generalised grid and projection methods for the construction of quasiperiodic tilings. *J. Phys. A: Math. Gen.*, 19(2):267, 1986.

[14] T.-L. Ho. Periodic quasicrystal. *Phys. Rev. Lett.*, 56:468–471, 1986.

[15] D. A. Rabson, T.-L. Ho, and N. D. Mermin. Aperiodic tilings with non-symmorphic space groups $p2^j gm$. *Acta Cryst. A*, 44:678–688, 1988.

[16] D. A. Rabson, T.-L. Ho, and N. D. Mermin. Space groups of quasicrystallographic tilings. *Acta Cryst. A*, 45:538–547, 1989.

[17] R. Lifshitz, A. Arie, and A. Bahabad. Photonic quasicrystals for nonlinear optical frequency conversion. *Phys. Rev. Lett.*, 95:133901, 2005.

[18] R. Lifshitz. The square Fibonacci tiling. *J. Alloys Compd.*, 342(1):186–190, 2002.

[19] A. Koga and S. Coates. Ferrimagnetically ordered states in the Hubbard model on the hexagonal golden-mean tiling. *Phys. Rev. B*, 105:104410, 2022.

[20] T. Matsubara, A. Koga, and S. Coates. Ferromagnetically ordered states in the hubbard model on the h 00 hexagonal golden-mean tiling. *Physical Review B*, 109(1):014413, 2024.

[21] Z. Zhang and S. C. Glotzer. Self-assembly of patchy particles. *Nano letters*, 4(8):1407–1413, 2004.

[22] S. Whitelam, I. Tamblyn, J. P. Garrahan, and P. H. Beton. Emergent rhombus tilings from molecular interactions with m-fold rotational symmetry. *Physical Review Letters*, 114(11):115702, 2015.

[23] C. Karner, C. Dellago, and E. Bianchi. Design of patchy rhombi: From close-packed tilings to open lattices. *Nano Letters*, 19(11):7806–7815, 2019.

[24] C. Karner, F. Müller, and E. Bianchi. A matter of size and placement: Varying the patch size of anisotropic patchy colloids. *International Journal of Molecular Sciences*, 21(22):8621, 2020.

[25] J. A. Millan, D. Ortiz, G. Van Anders, and S. C. Glotzer. Self-assembly of archimedean tilings with enthalpically and entropically patchy polygons. *ACS nano*, 8(3):2918–2928, 2014.

[26] J. A. Millan, D. Ortiz, and S. C. Glotzer. Effect of shape on the self-assembly of faceted patchy nanoplates with irregular shape into tiling patterns. *Soft Matter*, 11(7):1386–1396, 2015.

[27] D. Smith, J. S. Myers, C. S. Kaplan, and C. Goodman-Strauss. A chiral aperiodic monotile. *arXiv preprint arXiv:2305.17743*, 2023.

[28] B. A. Bernevig, C. Felser, and H. Beidenkopf. Progress and prospects in magnetic topological materials. *Nature*, 603(7899):41–51, 2022.

[29] S. H. Skjærvø, C. H. Marrows, R. L. Stamps, and L. J. Heyderman. Advances in artificial spin ice. *Nature Reviews Physics*, 2(1):13–28, 2020.

[30] J. Drisko, T. Marsh, and J. Cumings. Topological frustration of artificial spin ice. *Nature communications*, 8(1):14009, 2017.

[31] M. P. López-Sancho, F. de Juan, and M. A. Vozmediano. Magnetic moments in the presence of topological defects in graphene. *Physical Review B*, 79(7):075413, 2009.

[32] S. Ladak, D. Read, G. Perkins, L. Cohen, and W. Branford. Direct observation of magnetic monopole defects in an artificial spin-ice system. *Nature Physics*, 6(5):359–363, 2010.

[33] T. Cote, A. K. Petford-Long, and C. Phatak. Direct observation of magnetic ordering induced via systematic lattice disorder in artificial rhombus spin ices. *Nanoscale*, 15(27):11506–11516, 2023.

[34] B. Metcalf. Ground state spin orderings of the triangular ising model with the nearest and next nearest neighbor interaction. *Physics Letters A*, 46(5):325–326, 1974.

[35] M. Mekata. Antiferro-ferrimagnetic transition in triangular ising lattice. *Journal of the Physical Society of Japan*, 42(1):76–82, 1977.

[36] Z. Yan, R. Samajdar, Y.-C. Wang, S. Sachdev, and Z. Y. Meng. Triangular lattice quantum dimer model with vari-

able dimer density. *Nature Communications*, 13(1):5799, 2022.

[37] R. Moessner, S. L. Sondhi, and P. Chandra. Phase diagram of the hexagonal lattice quantum dimer model. *Physical Review B*, 64(14):144416, 2001.

[38] S. Singh, J. Lloyd, and F. Flicker. Hamiltonian cycles on ammann-beenker tilings. *arXiv preprint arXiv:2302.01940*, 2023.

[39] S. Singh and F. Flicker. Exact solution to the quantum and classical dimer models on the spectre aperiodic monotiling. *arXiv preprint arXiv:2309.14447*, 2023.

[40] C. Nisoli, R. Moessner, and P. Schiffer. Colloquium: Artificial spin ice: Designing and imaging magnetic frustration. *Reviews of Modern Physics*, 85(4):1473, 2013.

[41] S.-W. Hla. Scanning tunneling microscopy single atom/molecule manipulation and its application to nanoscience and technology. *Journal of Vacuum Science & Technology B: Microelectronics and Nanometer Structures Processing, Measurement, and Phenomena*, 23(4):1351–1360, 2005.

[42] J. Lagoute, K. Kanisawa, and S. Fölsch. Manipulation and adsorption-site mapping of single pentacene molecules on cu (111). *Physical Review B*, 70(24):245415, 2004.

[43] K. Kanisawa, S. Fölsch, et al. Quantum rings engineered by atom manipulation. *Physical review letters*, 123(6):066801, 2019.

[44] D. Wong, J. Velasco Jr, L. Ju, J. Lee, S. Kahn, H.-Z. Tsai, C. Germany, T. Taniguchi, K. Watanabe, A. Zettl, et al. Characterization and manipulation of individual defects in insulating hexagonal boron nitride using scanning tunnelling microscopy. *Nature nanotechnology*, 10(11):949–953, 2015.

[45] L.-H. Wu and X. Hu. Scheme for achieving a topological photonic crystal by using dielectric material. *Physical review letters*, 114(22):223901, 2015.

[46] S.-H. Kim, H.-Y. Ryu, H.-G. Park, G.-H. Kim, Y.-S. Choi, Y.-H. Lee, and J.-S. Kim. Two-dimensional photonic crystal hexagonal waveguide ring laser. *Applied Physics Letters*, 81(14):2499–2501, 2002.

[47] S. Kim and V. Gopalan. Strain-tunable photonic band gap crystals. *Applied Physics Letters*, 78(20):3015–3017, 2001.

[48] S. V. Li, Y. S. Kivshar, and M. V. Rybin. Toward silicon-based metamaterials. *ACS Photonics*, 5(12):4751–4757, 2018.

[49] R. Chaunsali, C.-W. Chen, and J. Yang. Experimental demonstration of topological waveguiding in elastic plates with local resonators. *New Journal of Physics*, 20(11):113036, 2018.

[50] D. Tallarico, N. V. Movchan, A. B. Movchan, and D. J. Colquitt. Tilted resonators in a triangular elastic lattice: chirality, bloch waves and negative refraction. *Journal of the Mechanics and Physics of Solids*, 103:236–256, 2017.

[51] C. Wolff, M. Steel, and C. Poulton. Formal selection rules for brillouin scattering in integrated waveguides and structured fibers. *Optics express*, 22(26):32489–32501, 2014.

[52] P. Zhao, K. Zhang, C. Zhao, L. Qi, and Z. Deng. In-plane wave propagation analysis for waveguide design of hexagonal lattice with koch snowflake. *International Journal of Mechanical Sciences*, 209:106724, 2021.

[53] D. Pérez and J. Capmany. Scalable analysis for arbitrary photonic integrated waveguide meshes. *Optica*, 6(1):19–27, 2019.

[54] K. H. Cho, J. Y. Kim, D.-G. Choi, K.-J. Lee, J.-H. Choi, and K. C. Choi. Surface plasmon-waveguide hybrid polymer light-emitting devices using hexagonal ag dots. *Optics Letters*, 37(5):761–763, 2012.

[55] M. Wang, W. Zhou, L. Bi, C. Qiu, M. Ke, and Z. Liu. Valley-locked waveguide transport in acoustic heterostructures. *Nature Communications*, 11(1):3000, 2020.

[56] J.-Q. Wang, Z.-D. Zhang, S.-Y. Yu, H. Ge, K.-F. Liu, T. Wu, X.-C. Sun, L. Liu, H.-Y. Chen, C. He, et al. Extended topological valley-locked surface acoustic waves. *Nature Communications*, 13(1):1324, 2022.

[57] P. Sinha and T. Mukhopadhyay. Programmable multiphysical mechanics of mechanical metamaterials. *Materials Science and Engineering: R: Reports*, 155:100745, 2023.

[58] T. Mukhopadhyay and S. Adhikari. Effective in-plane elastic moduli of quasi-random spatially irregular hexagonal lattices. *International Journal of Engineering Science*, 119:142–179, 2017.

[59] T. Mukhopadhyay and S. Adhikari. Stochastic mechanics of metamaterials. *Composite Structures*, 162:85–97, 2017.

[60] A. Valipour, M. H. Kargozarfard, M. Rakhshi, A. Yaghootian, and H. M. Sedighi. Metamaterials and their applications: an overview. *Proceedings of the Institution of Mechanical Engineers, Part L: Journal of Materials: Design and Applications*, 236(11):2171–2210, 2022.

[61] J. E. S. Socolar. Simple octagonal and dodecagonal quasicrystals. *Phys. Rev. B*, 39:10519–10551, 1989.

Appendix A: Vertices

1. *SEH* tiling duals

Figure A1 shows the dual of the SEH tilings, or, the edge removal guide to be overlaid onto a periodic triangular lattice - as discussed in the main text. The constituent tiles are coloured for the SEH_{00} and $SEH_{\frac{1}{2}\frac{1}{2}}$ duals ((a, b) respectively), and enlarged at the bottom of the figure. Out of interest, we note the similarity in structure of dual Figure A1(b) to various hexagonal and dodecagonal tilings [7, 61].

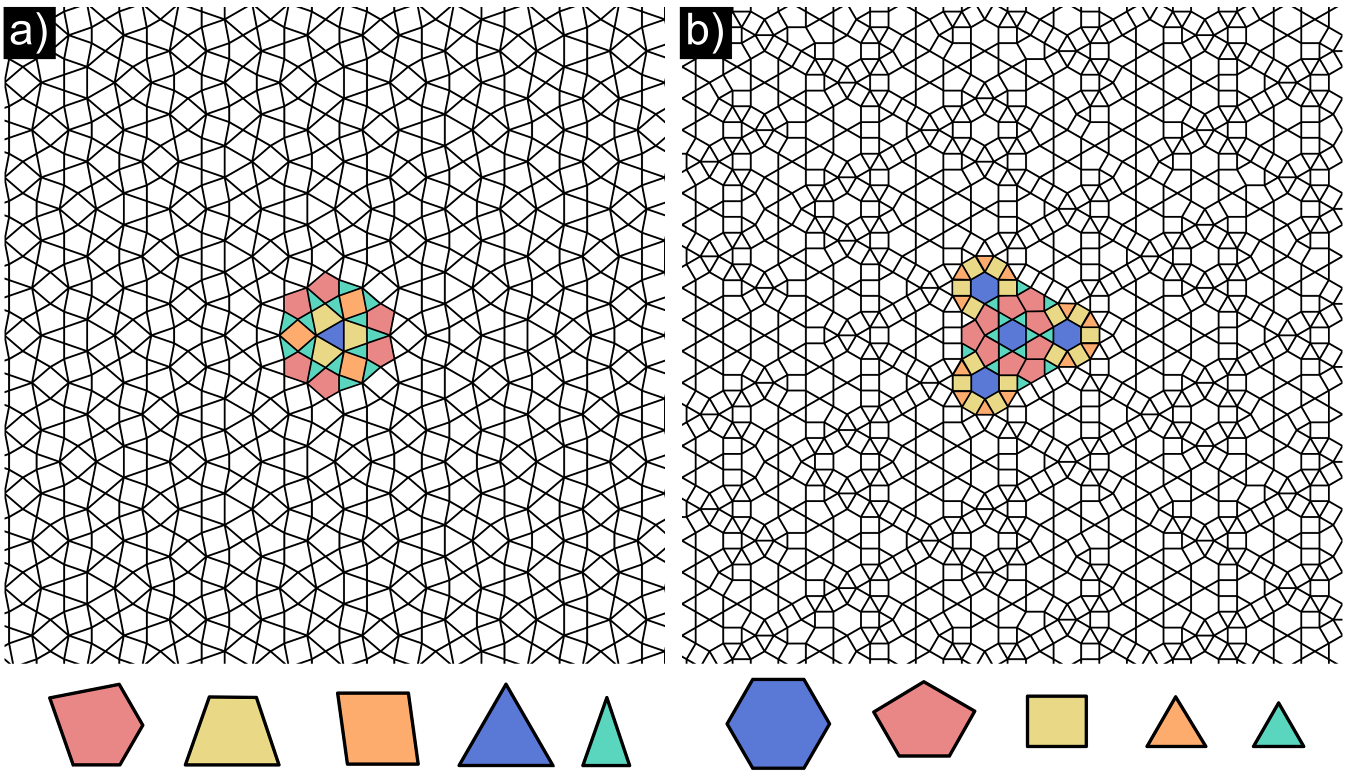

FIG. A1: Top: duals of the SEH_{00} and $SEH_{\frac{1}{2}\frac{1}{2}}$ tilings (**(a, b)** respectively), where the vertices of the duals correspond to the centre of the SEH tiles. Selected tiles are coloured to emphasise the tiling constituents. Bottom: enlarged versions of the dual tiles.

2. Radial distribution functions of n-vertices

Figures A2 and A3 show the radial distribution functions on each n-vertex of the SEH_{00} and $SEH_{\frac{1}{2}\frac{1}{2}}$ tiling, calculated for up to 5 distance units.

3. Vertex combinations

Figures A4 and A5 show the remaining bipartite vertex combinations of the SEH_{00} tilings. We do not show the combination which combines the 3-vertex and vacancy positions as one set, and the 4A-, 4B-, 5-, and 6-vertices as the other: this creates a periodic kagome-like lattice.

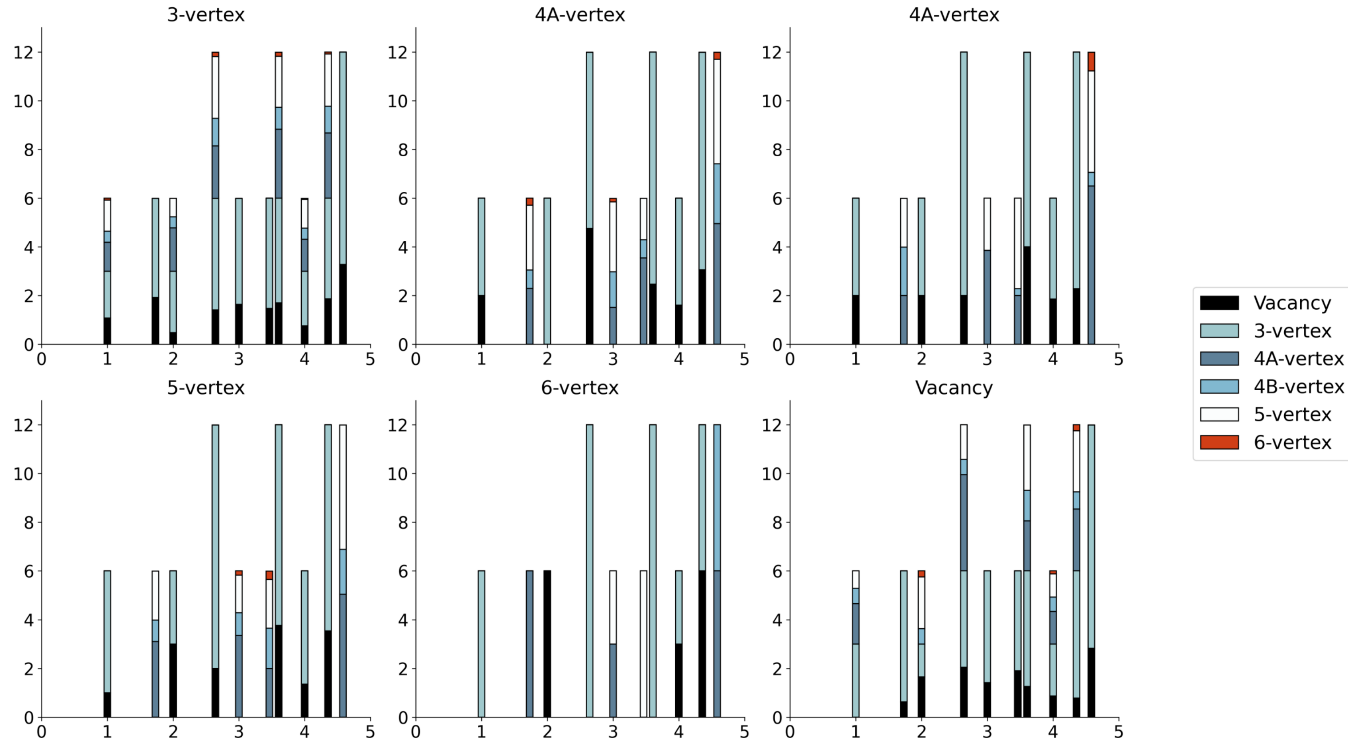

FIG. A2: Radial distribution functions on each n-vertex of the SEH_{00} tiling.

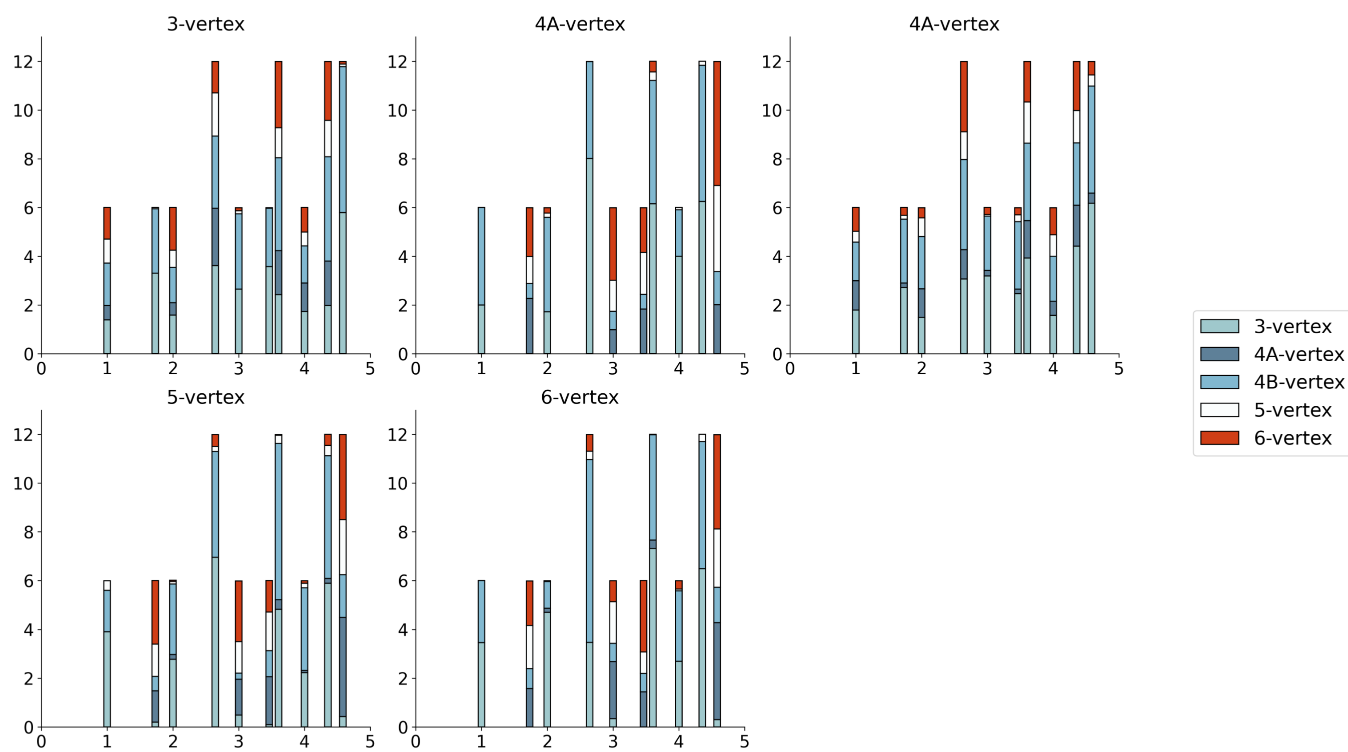

FIG. A3: Radial distribution functions on each n-vertex of the $SEH_{\frac{1}{2}\frac{1}{2}}$ tiling.

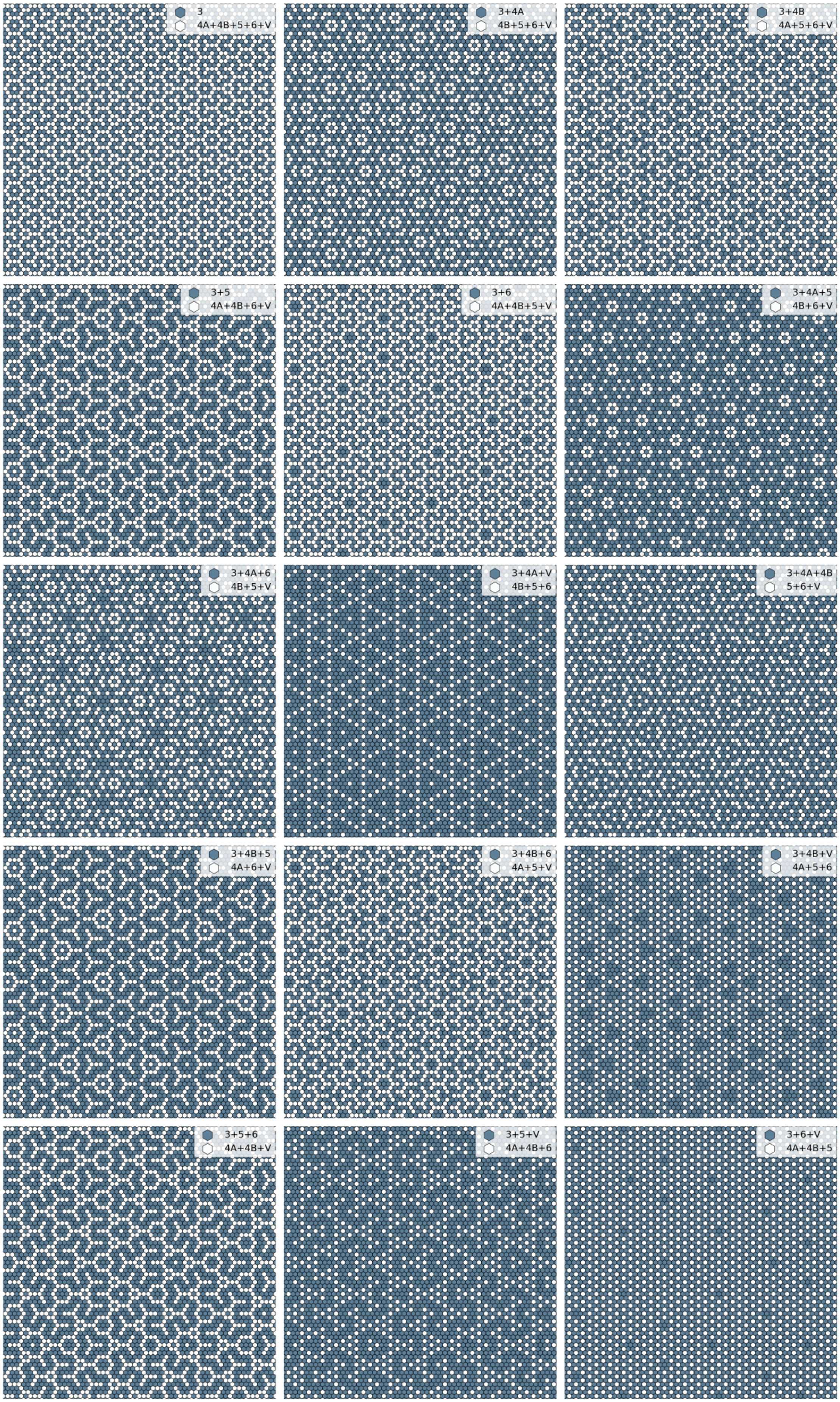

FIG. A4: First fifteen vertex combinations of the SEH_{00} tiling.

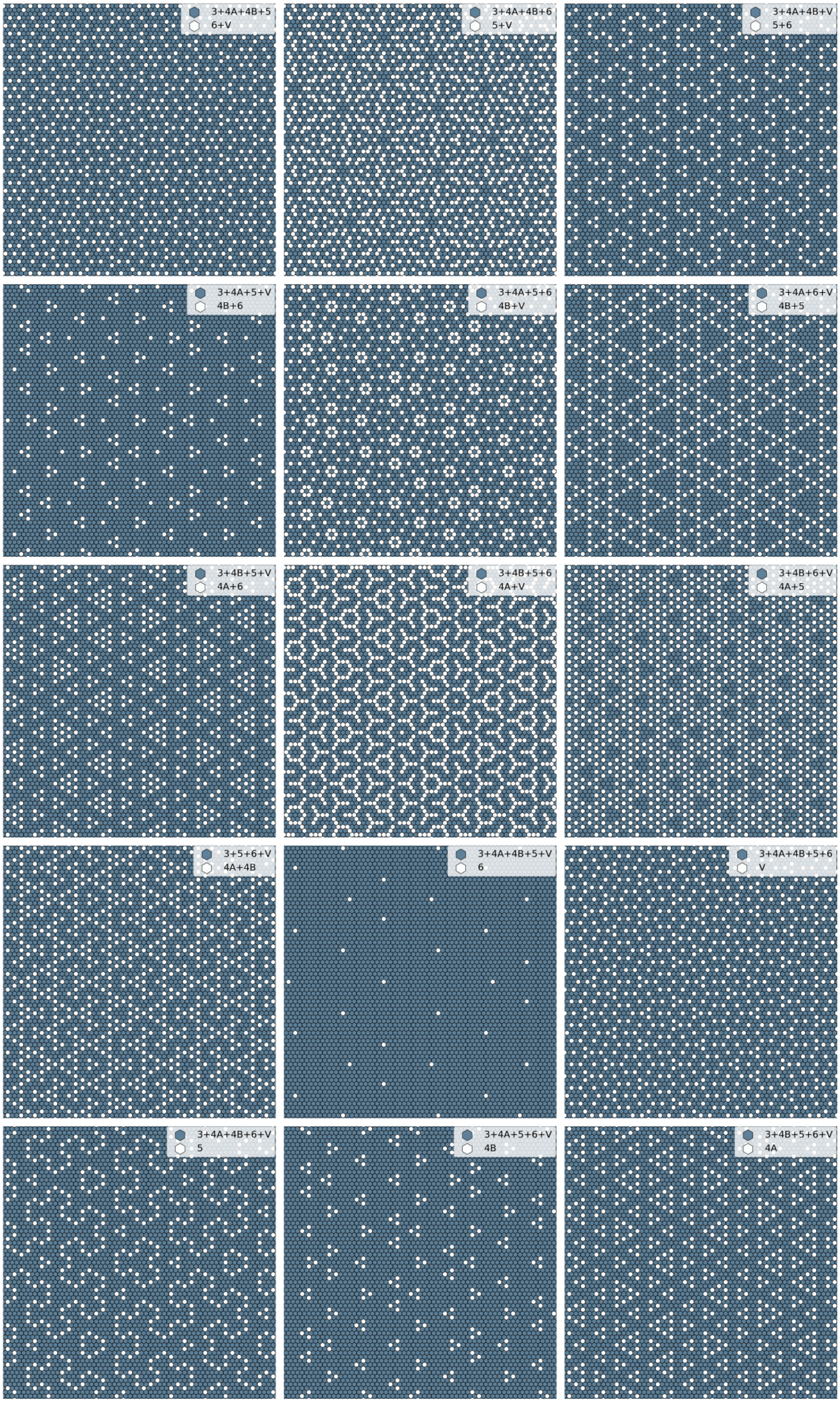

FIG. A5: Second fifteen vertex combinations of the SEH_{00} tiling.

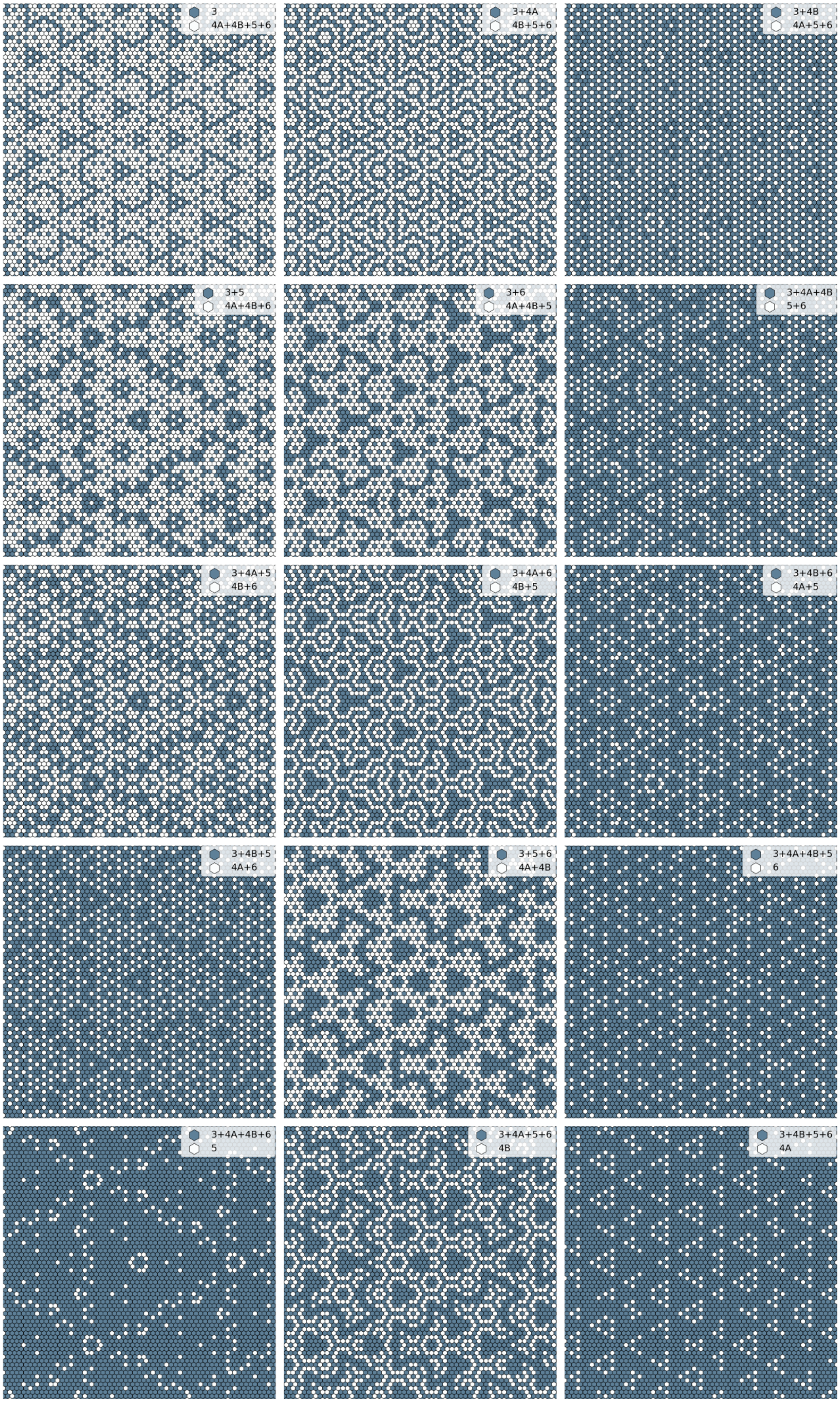

FIG. A6: Vertex combinations of the $SEH_{\frac{1}{2}\frac{1}{2}}$ tiling.

4. Arbitrary scaling ratios between $\mathbf{k}^{1-3}$ and $\mathbf{k}^{4-6}$

Figure A7 shows the n-vertex distributions for the SEH_{00} (a-c) and $SEH_{\frac{1}{2}\frac{1}{2}}$ (d-f) tilings where the scaling ratio between $\mathbf{k}^{1-3}$ and $\mathbf{k}^{4-6}$ has been arbitrarily chosen as $\frac{1}{\sqrt{2}}$ (a,d), $\sqrt{7}-2$ (b,e), and $\sqrt{\pi}$ (c,f) respectively.

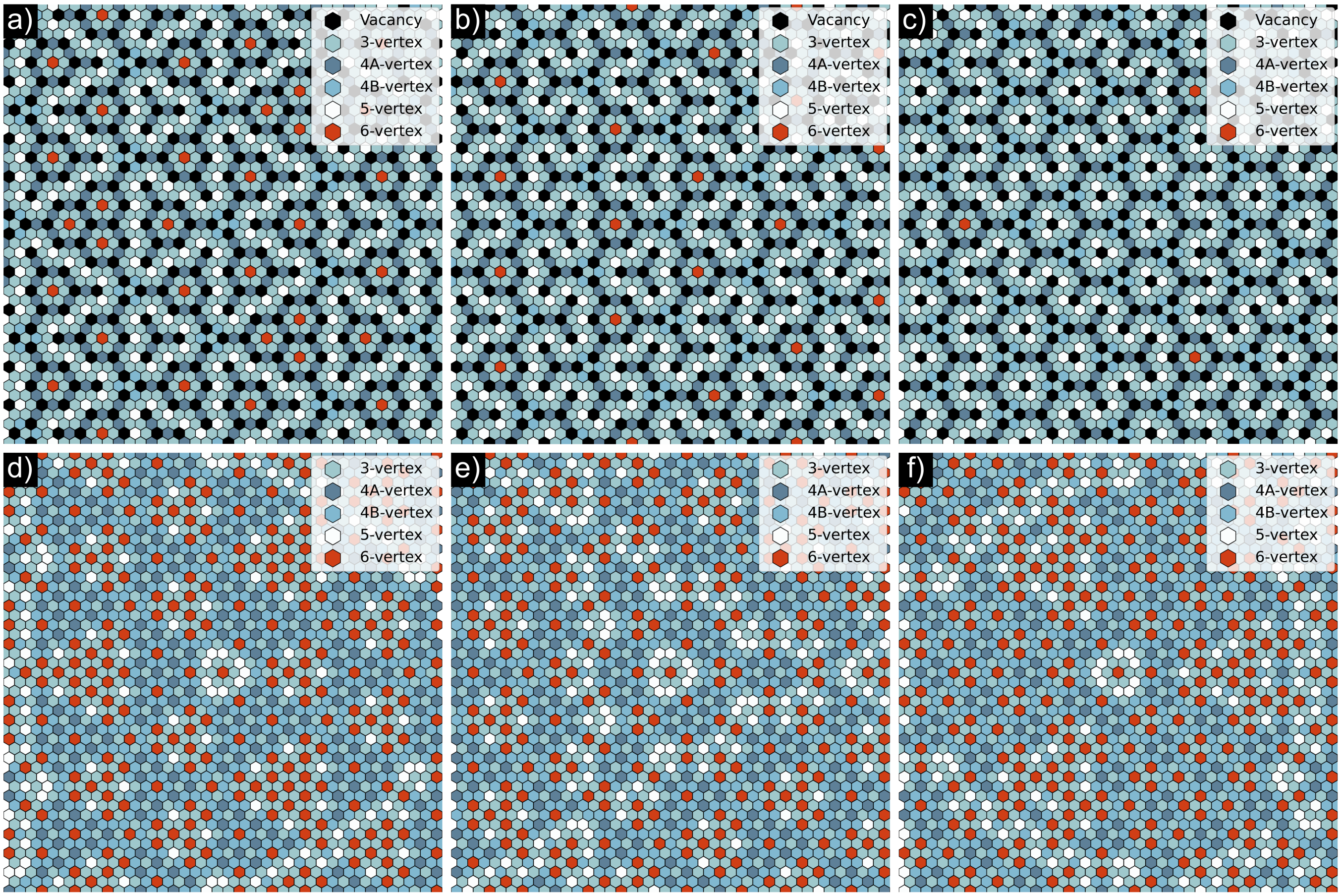

FIG. A7: Vertex distributions for the SEH_{00} tiling **(a-c)** and $SEH_{\frac{1}{2}\frac{1}{2}}$ tilings **(d-f)** with different scaling ratios between the grid vectors $\mathbf{k}^{1-3}$ and $\mathbf{k}^{4-6}$ which define tile placement. **(a,d)** are scaled by $\frac{1}{\sqrt{2}}$, **(b,d)** by $\sqrt{7}-2$, and **(c,f)** by $\sqrt{\pi}$.

Appendix B: Random defect model

Figure A8(a) shows the spin texture of a randomly selected defect lattice for when $J_1 \equiv J_2 \equiv -1$. Green hexagons have spin up, purple have spin down. Figure A8(b) shows the corresponding random tiling from this defect structure. Hexagons are centred on the vacancies; and the rhombic and triangle tiles fill the remaining spaces randomly.

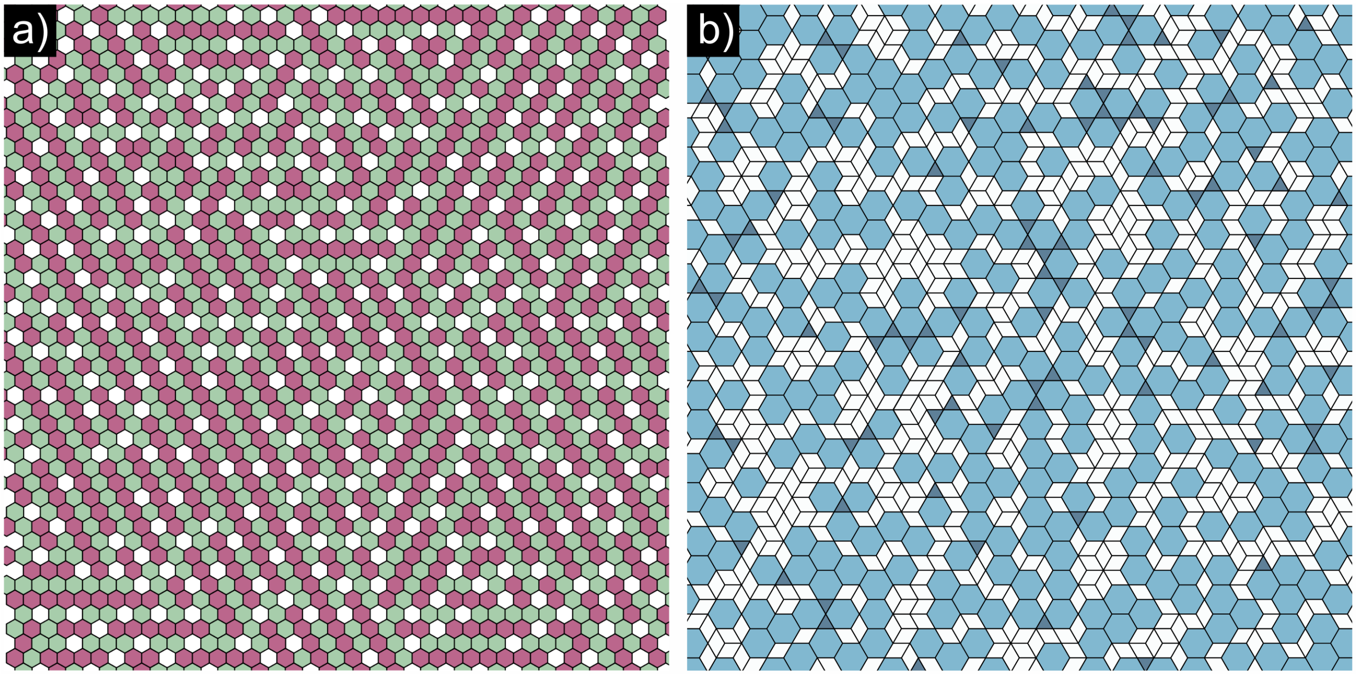

FIG. A8: **(a)** Spin structure of a defect lattice where $J_1 \equiv J_2 \equiv -1$. Green hexagons are spin up, purple are spin down. **(b)** shows the tiling structure of the defect lattice.